Turbulent mixing of passive scalar near turbulent and non-turbulent interface in mixing layers

Cite as: Phys. Fluids **27**, 085109 (2015); https://doi.org/10.1063/1.4928199
Submitted: 21 January 2015 • Accepted: 23 July 2015 • Published Online: 21 August 2015

T. Watanabe, Y. Sakai, K. Nagata, et al.

PHYSICS OF FLUIDS **27**, 085109 (2015)

Turbulent mixing of passive scalar near turbulent and non-turbulent interface in mixing layers

T. Watanabe,[1,a)] Y. Sakai,[1] K. Nagata,[2] Y. Ito,[1] and T. Hayase[3]
[1]*Department of Mechanical Science and Engineering, Nagoya University, Nagoya, Japan*
[2]*Department of Aerospace Engineering, Nagoya University, Nagoya, Japan*
[3]*Institute of Fluid Science, Tohoku University, Sendai, Japan*

(Received 21 January 2015; accepted 23 July 2015; published online 21 August 2015)

A direct numerical simulation of a temporally developing mixing layer with a passive scalar transport is performed for various Schmidt numbers (Sc = 0.25, 1, 4, and 8). Turbulent mixing is investigated near the turbulent/non-turbulent interface (TNTI), which is a layer consisting of the turbulent sublayer (TSL) and viscous superlayer (VSL). The irrotational boundary, which is close to the outer edge of the TNTI layer, is detected as the isosurface of small vorticity magnitude. The movement of fluid elements relative to the irrotational boundary movement is analyzed. Once the non-turbulent fluid is entrained into the VSL across the irrotational boundary by the viscous diffusion of vorticity, the fluid moves away from the irrotational boundary in the VSL in the normal direction of the irrotational boundary. After the fluid reaches the TSL, it is transported in the tangential direction of the irrotational boundary and is mixed with the fluid coming from the turbulent core (TC) region. The boundary between the TSL and VSL roughly separates the region (VSL) mostly consisting of the fluid entrained from the non-turbulent flow from the region (TSL) where the fluids from both the TC and non-turbulent regions coexist. Therefore, the scalar value in the VSL is close to the non-turbulent value especially for high Sc cases. Because of a large difference in the scalar between the TSL and VSL, a peak value of the conditional mean scalar dissipation rate appears near the boundary between the TSL and VSL independently of Sc. [http://dx.doi.org/10.1063/1.4928199]

I. INTRODUCTION

Turbulent mixing of a passive scalar[1] is an important phenomenon that is observed in various flows in engineering equipment and the environment. For instance, in chemical reactors, the characteristics of reactions are largely affected by scalar transport from turbulence and mixing at the molecular level.[2,3] Thus, predicting and controlling the scalar transport process is desired when designing engineering equipment. The Schmidt number $Sc \equiv \nu/D$ (ν: kinematic viscosity and D: molecular diffusivity) is an important parameter which characterizes passive scalar mixing in turbulent flows. The smallest scale of the scalar fluctuation changes depending on the Schmidt number. For the mixing of diffusive matter in liquid flows, the Schmidt number is of the order of 10^2–10^3. In contrast, the mixing in gaseous flows is characterized by a much smaller Schmidt number ($Sc \sim 1$). The dependence of the scalar transport process on the Schmidt number should be investigated in order to understand turbulent mixing.

In free shear flows such as wakes, jets, and mixing layers, turbulent fluids inside these flows are separated from non-turbulent fluids by a layer called the turbulent/non-turbulent interface (TNTI).[4] The TNTI consists of the turbulent sublayer (TSL)[4] and the viscous superlayer (VSL).[5,6] In the VSL, vorticity is transported by viscous diffusion from turbulent regions, whereas the inviscid process is important to the vorticity dynamics in the TSL.[7] The geometric features of the TNTI have been

a)watanabe.tomoaki@c.nagoya-u.jp

investigated through direct numerical simulation (DNS). da Silva and Taveira[8] showed that the thickness of the TNTI in a planar jet is almost equal to the radius of large vorticity structures near the interface. The TNTI appears along the vortical structure in the turbulent region;[9] therefore, the vorticity near the interface is tangentially aligned with the interface.[10] Free shear flows spread by converting non-turbulent fluids near the TNTI into turbulent ones; thus, the non-turbulent fluids are entrained into the turbulent region. Previous studies on the TNTI also investigated the entrainment of non-turbulent fluids in experiments and numerical simulations. These studies showed that small-scale processes have an important role in the entrainment.[11–15] However, the total entrainment process can be significantly affected by large-scale characteristics because the non-turbulent fluids are advected by the large-scale motions.[16] Chauhan *et al.* showed that the entrainment in the boundary layer at high Reynolds numbers is characterized by two different length scales.[17]

In experiments, measuring the vorticity is quite difficult; therefore, other quantities such as the passive scalar and kinetic energy[17–19] are often used to detect the TNTI instead of the vorticity. A diffusive dye is added into a turbulent fluid, or the fluid is slightly heated; the concentration of the dye or temperature is then used as a marker of the turbulent region in experiments[20–23] and large eddy simulations.[24] For detection of the TNTI based on the passive scalar, the isosurface of the scalar is often used for investigating the characteristics of the flow and scalar fields near the TNTI.

The turbulent mixing of a passive scalar is considered to be caused by the entrainment, stirring, and molecular diffusion.[1] In free shear flows, the entrainment of the non-turbulent fluids is accompanied by the growth of enstrophy in the non-turbulent region. Thus, the turbulent mixing near the TNTI is related to the enstrophy transport process, which has been investigated in previous studies.[7,14,15,25–30] Because of the viscous diffusion of vorticity, the non-turbulent fluid near the TNTI acquires vorticity and becomes turbulent. Thus, the non-turbulent fluid is locally entrained into the turbulent region (local entrainment). However, the scalar transport itself is dominated by the different processes from the enstrophy transport. It was shown that the interface propagation and molecular diffusion contribute to the change in the passive scalar value for $Sc = 1$ near the TNTI in a planar jet by analyzing the scalar transport equation in the local frame moving with the TNTI.[29]

In this study, we investigate the turbulent mixing of a passive scalar and the dependence on the Schmidt number of the passive scalar characteristics near the TNTI. We perform a DNS of a temporally developing mixing layer with the transport of multiple passive scalars with different Sc. The location of the TNTI is detected by using the isosurface of small vorticity magnitude which is very close to the outer edge of the TNTI layer. In this way, we can find the VSL and TSL inside the isosurface of vorticity magnitude. The scalar statistics near the TNTI are used for investigating the Sc dependence of the location of the scalar isosurface for detecting the TNTI, which will be useful information in experimental studies on the TNTI using the scalar isosurface instead of the enstrophy isosurface. Our previous study[29] used the scalar transport equation in the frame moving with the enstrophy isosurface for investigating the temporal variations in the passive scalar near the TNTI rather than the scalar transport, which is well represented by the scalar flux in the transport equation. In this study, the DNS results are used for detail analysis on the scalar fluxes in the scalar transport equation, which are determined by the movement of the fluid element relative to the irrotational boundary and the molecular diffusion effect. Finally, we will show that the turbulent mixing near the TNTI is caused by three different processes: the local entrainment of the non-turbulent fluid element in the VSL, the transport by the turbulent motions in the TSL, and the molecular diffusion which exchanges the scalar between the VSL and TSL. The scalar statistics for high Sc cases are also used for examining whether fluids within the TNTI come from the turbulent core (TC) region or the non-turbulent region, which will be important in considering the turbulence characteristics across the TNTI layer.

II. DIRECT NUMERICAL SIMULATION OF TEMPORALLY DEVELOPING MIXING LAYER

A. Numerical method and computational parameters

A DNS is performed for a temporally developing incompressible mixing layer[31–33] with the transfer of the passive scalar ϕ. The numerical methods and simulation conditions are described here. The origin of the coordinate system is located at the center of the computational domain. The streamwise,

lateral, and spanwise directions are represented by x, y, and z, respectively. The flow and scalar fields are periodic in the x and z directions. The initial velocity profiles are generated by superimposing fluctuating components to the mean velocity profile. The initial mean streamwise velocity profile U_0 is given by

$$U_0(x, y, z) = \frac{\Delta U_0}{2} \tanh\left(\frac{2y}{\delta_{\omega 0}}\right). \tag{1}$$

Here, ΔU_0 is the initial velocity difference and $\delta_{\omega 0}$ is the initial vorticity thickness defined by $\delta_{\omega 0} = \Delta U_0/(\partial U_0/\partial y)_{\max}$. The initial lateral and spanwise mean velocities are $V_0 = W_0 = 0$. The velocity fluctuations are generated by a diffusion process which converts the random noise into fluctuations that possess the required length scales.[34] Statistically homogeneous and isotropic fluctuations are added to the mean velocity profile. The integral length scale and rms value of the initial velocity fluctuations are $\delta_{\omega 0}/4$ and $0.01\Delta U_0$, respectively. For the initial scalar field, the following profile is used without any scalar fluctuations:

$$\phi_0(x, y, z) = \frac{\phi_1 + \phi_2}{2} + \frac{\phi_1 - \phi_2}{2} \tanh\left(\frac{2y}{\delta_{\omega 0}}\right). \tag{2}$$

Here, ϕ_1 and ϕ_2 are the scalar values on the upper and lower sides of the mixing layer, respectively, and we set their values to $\phi_1 = 1$ and $\phi_2 = 0$.

The governing equations are the continuity equation, Navier–Stokes equations, and transport equation for the passive scalar ϕ. These are written as follows:

$$\frac{\partial U_j}{\partial x_j} = 0, \tag{3}$$

$$\frac{\partial U_i}{\partial t} + \frac{\partial U_j U_i}{\partial x_j} = -\frac{\partial p}{\partial x_i} + \nu \frac{\partial^2 U_i}{\partial x_j \partial x_j}, \tag{4}$$

$$\frac{\partial \phi}{\partial t} + \frac{\partial U_j \phi}{\partial x_j} = D \frac{\partial^2 \phi}{\partial x_j \partial x_j}, \tag{5}$$

where U_i is the instantaneous velocity component in the i direction, p is the instantaneous pressure divided by the density, ν is the kinematic viscosity, and D is the diffusivity coefficient for ϕ. The size of the computational domain is $L_x \times L_y \times L_z = 22\pi\delta_{\omega 0} \times 17.5\pi\delta_{\omega 0} \times 7\pi\delta_{\omega 0}$. In the DNS, the governing equations are non-dimensionalized by ΔU_0 and $\delta_{\omega 0}$. Therefore, the time t is non-dimensionalized by the reference time $T_{\text{ref}} = \delta_{\omega 0}/\Delta U_0$. The initial Reynolds number based on ΔU_0 and $\delta_{\omega 0}$ is $Re = \Delta U_0 \delta_{\omega 0}/\nu = 380$. The passive scalar is computed for four different Schmidt numbers: $Sc = \nu/D = 0.25$, 1, 4, and 8. The different passive scalars are computed for the same velocity field.

In this study, we use a DNS code based on the finite difference method in Suzuki *et al.*[35] The fully conservative fourth-order central difference scheme proposed by Morinishi *et al.*[36] is used for spatial discretization in the x and z directions, and the fully conservative second-order central difference scheme[36] is used in the y direction. The continuity equation and Navier–Stokes equations are solved by using the fractional step method. The Poisson equation for pressure is solved by using the diagonal matrix algorithm along the y direction and the fast Fourier transform along the periodic (x and z) directions. The governing equations are temporally integrated using the explicit/implicit hybrid scheme based on the Crank–Nicolson method and the third-order Runge–Kutta method.[37] The former is used for the viscous and molecular diffusion terms and the latter is used for the other terms. At the lateral boundaries, the y direction derivative of the velocity is set to 0, and $\phi = \phi_1$ ($= \phi_2$) is imposed at $y = L_y/2$ ($= -L_y/2$). The computational domain is represented by $N_x \times N_y \times N_z = 1024 \times 600 \times 512$ computational grid points. The grid is equidistant in the x and z directions. In the y direction, a fine grid is used near the center of the mixing layer, and the grid is stretched near the lateral boundaries. The minimum resolution in the y direction is $0.061\delta_{\omega 0}$ at $y = 0$ and the maximum resolution is $0.23\delta_{\omega 0}$ at $y = \pm L_y/2$, which is far from the mixing layer.

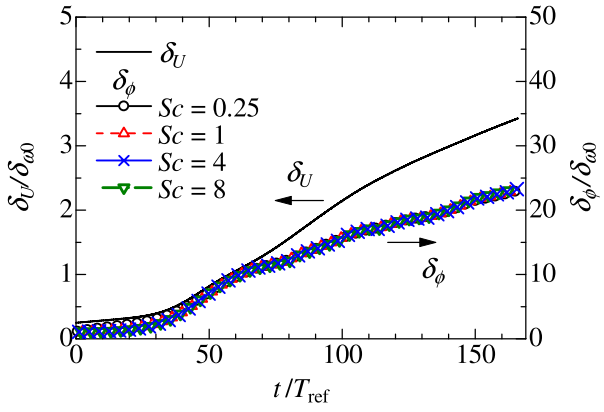

FIG. 1. Development of momentum thickness and thickness of mean scalar profile.

B. Conventional statistics of temporally developing mixing layer

We calculate the conventional statistics from an instantaneous field by taking the average on a x-z plane at each lateral location; this averaged value is denoted by $\langle\ \rangle$. The momentum thickness δ_U is defined by

$$\delta_U = \int_{-L_y/2}^{L_y/2} \frac{(U_1 - \langle U\rangle)(\langle U\rangle - U_2)}{(\Delta U_0)^2} dy. \tag{6}$$

Here, U_1 and U_2 are the values of $\langle U\rangle$ at $y = L_y/2$ and $-L_y/2$, respectively. The thickness of the mean scalar profile δ_ϕ is defined by $\delta_\phi = 2(y_{\langle\phi\rangle=0.75} - y_{\langle\phi\rangle=0.25})$, where $y_{\langle\phi\rangle=0.75}$ and $y_{\langle\phi\rangle=0.25}$ are the lateral locations of $\langle\phi\rangle = 0.75$ and 0.25, respectively. Figure 1 shows the development of δ_U and δ_ϕ for different Sc. Until $t/T_{\rm ref} = 40$, δ_U and δ_ϕ slowly increase and then begin to rapidly increase. A similar development in δ_U was seen in the DNS results of Tanahashi *et al.*[32] Although the development of δ_ϕ slightly depends on the Schmidt number until $t/T_{\rm ref} = 40$, this dependence cannot be seen after the mixing layer is fully developed. Figure 2 shows the lateral profiles of $\langle U\rangle$ and $\langle\phi\rangle$. For $\langle U\rangle$ and $\langle\phi\rangle$, the mixing layer reaches the self-similar state before $t/T_{\rm ref} = 144.0$, and the profiles of $\langle U\rangle$ agree well with the previous DNS results.[32,33]

In the present study, the instantaneous fields at $t/T_{\rm ref} = 155.0, 157.5, 160.0, 162.5$, and 165.0 are used for the analysis of the TNTI, and the statistics are obtained by taking the average of these five time steps. The statistical properties of the turbulence hardly change during this time interval. On the center of the mixing layer ($y = 0$) at $t/T_{\rm ref} = 165.0$, the Taylor microscale λ_x based on the streamwise velocity is $1.58\delta_{\omega 0}$, the Kolmogorov length scale $\eta = (\nu^3/\epsilon)^{1/4}$ is $7.69 \times 10^{-2}\delta_{\omega 0}$, and the turbulent Reynolds number $Re_\lambda = \langle u^2\rangle^{1/2}\lambda_x/\nu$ is 99. Here, $\lambda_i = \sqrt{\langle u_i^2\rangle/\langle(\partial u_i/\partial x_i)^2\rangle}$ (no summation with

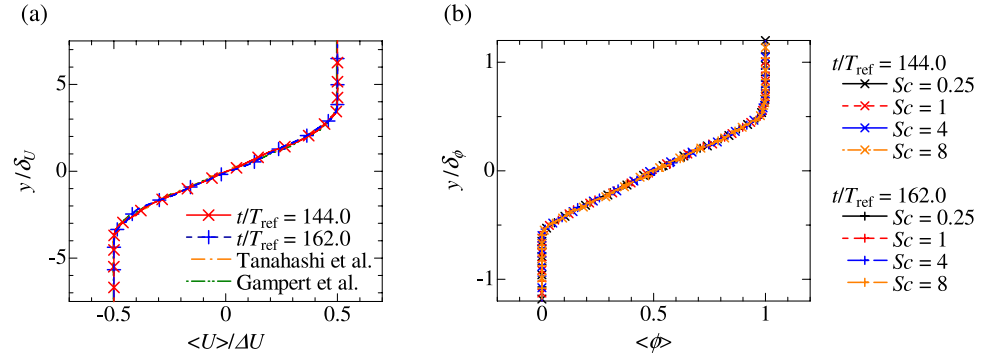

FIG. 2. Self-similar profiles of (a) mean streamwise velocity and (b) mean scalar for different Sc at $t/T_{\rm ref} = 144.0$ and 162.0. The mean streamwise velocity profiles obtained by Tanahashi *et al.*[32] and Gampert *et al.*[33] are also shown in (a).

respect to i) is the Taylor microscale, $u_i = U_i - \langle U_i \rangle$ is the fluctuating component of U_i, and ϵ is the dissipation rate of turbulent kinetic energy. The smallest scale of the scalar fluctuation decreases as Sc increases. At $t/T_{\mathrm{ref}} = 165.0$, the computational grid sizes in the x, y, and z directions at $y = 8\delta_{\omega 0}$ are $\Delta x = 1.86\eta_{\mathrm{B}}$, $\Delta y = 1.92\eta_{\mathrm{B}}$, and $\Delta z = 1.18\eta_{\mathrm{B}}$ for $Sc = 8$, respectively. Here, $\eta_{\mathrm{B}} = \eta/Sc^{1/2}$ is the Batchelor scale. These grid sizes correspond to $\Delta x = 0.66\eta$, $\Delta y = 0.68\eta$, and $\Delta z = 0.42\eta$, respectively.

III. RESULTS AND DISCUSSION

A. Detection of turbulent/non-turbulent interface and conditional analysis

The isosurface of normalized vorticity magnitude $|\omega|/(\Delta U_0/\delta_U) = \omega_{\mathrm{th}}$ is used for investigating the TNTI. The TNTI is a thin layer with finite thickness,[4] and the location of the isosurface of vorticity magnitude changes within the TNTI layer depending on the threshold ω_{th}. In this study, ω_{th} is chosen so that the isosurface of ω_{th} is located very close to the outer edge of the TNTI layer by using small ω_{th}. We refer to this isosurface close to the outer edge of the TNTI as the *irrotational boundary* and define the region of $|\omega|/(\Delta U_0/\delta_U) \geq \omega_{\mathrm{th}}$ as the turbulent region. Here, we introduced the term, *irrotational boundary*, for distinguishing the isosurface of the constant vorticity magnitude, which is an infinitely thin surface, from the layer called the TNTI. As in previous studies,[6,15] the threshold ω_{th} is determined from the volume fraction of the detected turbulent region (V_{T}). Figure 3(a) shows V_{T} and $dV_{\mathrm{T}}/d\omega_{\mathrm{th}}$ as functions of the threshold ω_{th}. The dependence of V_{T} on ω_{th} is similar to previous DNS studies.[15,29] The turbulent volume largely increases for $\omega_{\mathrm{th}} < 0.04$ as ω_{th} decreases because of weak vorticity outside the mixing layer. However, for $0.06 \leq \omega_{\mathrm{th}} \leq 0.1$, the dependence of V_{T} on ω_{th} is small and there is a plateau-like region of $V_{\mathrm{T}} \approx 0.3$ as confirmed from V_{T} and $dV_{\mathrm{T}}/d\omega_{\mathrm{th}}$; thus, we use $\omega_{\mathrm{th}} = 0.08$. The enstrophy dynamics changes between the TSL and VSL. In Subsection III B,we will confirm that the inviscid process is negligible in the enstrophy dynamics at the isosurface of $|\omega|/(\Delta U_0/\delta_U) = 0.08$ and the isosurface can be used as the irrotational boundary, which is close to the outer edge of the VSL. In this definition of the irrotational boundary, the VSL and TSL are located inside the isosurface of the vorticity magnitude.

The statistics conditioned on the distance from the irrotational boundary are analyzed. We introduce the local coordinate y_{I} as shown in Fig. 3(b). The location of the irrotational boundary is represented by $y_{\mathrm{I}} = 0$ in the local coordinate system. Here, y_{I} is taken to be normal to the irrotational boundary, and the turbulent fluid is on the side of the negative y_{I}. The direction normal to the irrotational boundary is the enstrophy gradient direction. We use the unit normal vector $\mathbf{n} = -\nabla\omega^2/|\nabla\omega^2|$ to determine the local coordinate y_{I}. The conditional statistics conditioned on y_{I} are calculated for both the turbulent and non-turbulent sides of the irrotational boundary; the conditional average is denoted by $\langle\ \rangle_{\mathrm{I}}$. When the conditional statistics are calculated for an irrotational boundary, other TNTI can appear on y_{I}. The characteristics of the flow field drastically vary near the TNTI, and we confirmed that the width of this variation in the conditional mean vorticity magnitude is of the order of the

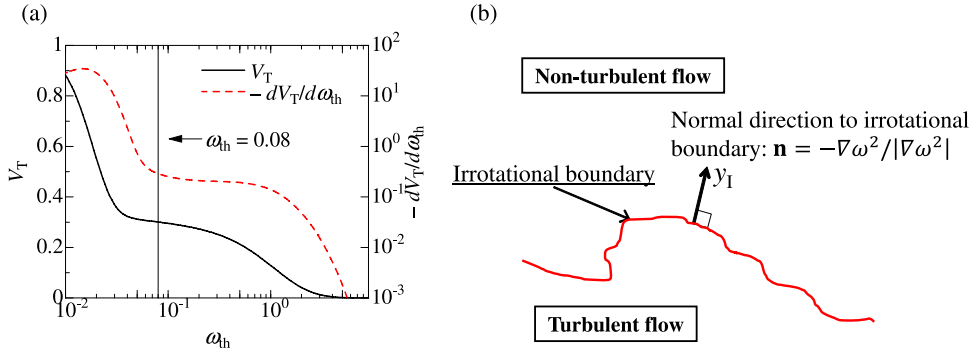

FIG. 3. (a) Volume fraction of turbulent region (V_{T}) and $dV_{\mathrm{T}}/d\omega_{\mathrm{th}}$ as functions of the threshold ω_{th}. (b) Definition of local coordinate y_{I} used for calculating conditional statistics conditioned on the distance from the irrotational boundary.

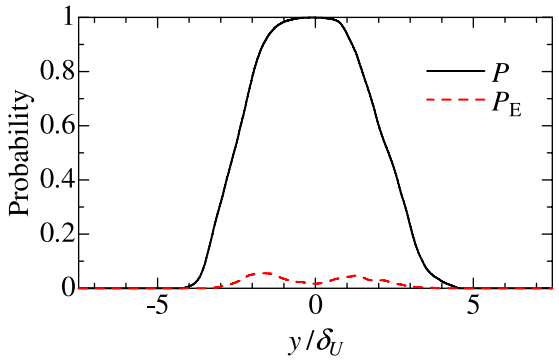

FIG. 4. Probabilities that a fluid is located within the irrotational boundary envelope (P) and that an engulfed fluid is found (P_E) calculated as a function of y.

Taylor microscale in the mixing layer. This width of the vorticity jump is close to that observed in planar jets.[29,30,38] Therefore, when other irrotational boundaries appear on the local coordinate y_I, the region within λ away from the other irrotational boundaries is not used for calculating the conditional statistics, where λ is the Taylor microscale $\lambda = (\lambda_x + \lambda_y + \lambda_z)/3$ at $y = 0$. Note that the existence of other irrotational boundaries is only examined on y_I.

We calculate the probability P_E that an engulfed fluid is found as a function of y according to Westerweel *et al.*[13] Here, an engulfed fluid is defined as the fluid which is within the irrotational boundary envelope and has a vorticity magnitude smaller than the threshold ω_{th}. We also calculate the probability P that a fluid is located within the envelope. The probabilities P and P_E are compared in Fig. 4. Although the amount of engulfed fluid is very small, the engulfed fluid can be found even at the centerline as in a round jet.[13]

B. Enstrophy transport near turbulent/non-turbulent interface

The enstrophy transport mechanism is important to the TNTI characteristics. First, we confirm that the conditional statistics related to the enstrophy are similar to those in previous studies. The enstrophy evolves according to the following transport equation:

$$\frac{D\omega^2/2}{Dt} = \omega_i S_{ij} \omega_j + \nu \nabla^2(\omega^2/2) - \nu \nabla \omega_i \cdot \nabla \omega_i. \tag{7}$$

The first, second, and third terms on the right hand side are for the production (P_ω), viscous diffusion (D_ω), and viscous dissipation (ϵ_ω), respectively. Figure 5(a) shows the conditional averages of $\omega^2/2$, P_ω, D_ω, and ϵ_ω. The distance y_I is normalized by the Kolmogorov length scale η at $y = 0$. The enstrophy increases from the irrotational boundary ($y_I = 0$) toward the turbulent region. At $y_I/\eta = -14$, the conditional mean enstrophy reaches the value in the TC region ($\langle\omega^2/2\rangle_I/(\Delta U_0/\delta_{\omega 0})^2 = 0.1$). The similar profile of $\langle\omega^2/2\rangle_I$ can be seen in the temporally developing planar jet[7] and mixing layer.[33] The conditional mean profile of Eq. (7) is also quite similar to the DNS results of the planar jets.[7,30] Very close to the irrotational boundary, the enstrophy growth is caused by the viscous diffusion, and the production term is negligible; this indicates the existence of the VSL. At $y_I = 0$, the viscous diffusion term is also small, and thus, the isosurface of $|\omega|\delta_U/\Delta U_0 = 0.08$ is located very close to the outer edge of the TNTI. When larger ω_{th} is used, the isosurface is located in the VSL region closer to the TSL, and the viscous diffusion and production terms have much larger values. In the conditional mean profiles, the production term becomes equal to the viscous diffusion term ($\langle P_\omega\rangle_I = \langle D_\omega\rangle_I$) at $y_I/\eta = -4.9$. Thus, when we assume that the irrotational boundary is located at the outer edge of the VSL, the thickness of the region in which the viscous diffusion is predominant over the inviscid production within the TNTI is about 5η in the mean profile. Although this thickness is obtained from the mean profile, it is close to the mean VSL thickness obtained by Taveira and da Silva.[7] Thus, the region $-14 \le y_I/\eta \le -5$ corresponds to the TSL, where the inviscid production has a greater contribution to the increase in the enstrophy than the viscous diffusion. In this region, the enstrophy

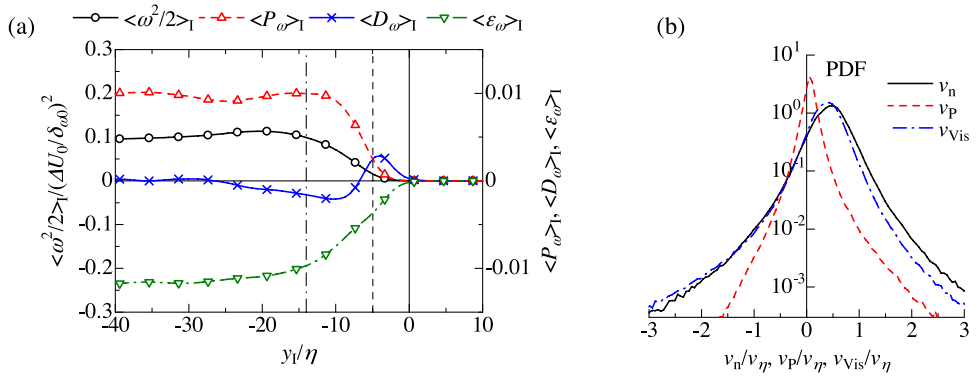

FIG. 5. Enstrophy transport characteristics near TNTI. (a) Conditional average of enstrophy and enstrophy transport equation. The vertical broken line shows $y_I/\eta = -4.9$, which is the location of $\langle P_\omega \rangle_I = \langle D_\omega \rangle_I$. The vertical dashed-dotted line shows $y_I/\eta = -14$, at which the conditional mean enstrophy reaches the value in the turbulent core region ($\langle \omega^2/2 \rangle_I/(\Delta U_0/\delta_{\omega 0})^2 = 0.1$). The enstrophy transport equation is normalized by $\delta_{\omega 0}$ and ΔU_0. (b) Probability density function of propagation velocity of irrotational boundary. The propagation velocity is normalized by the Kolmogorov velocity $v_\eta = (\epsilon\nu)^{1/4}$ at $y = 0$.

is adjusted between the TC and non-turbulent regions. It was shown that the thickness of the buffer region between the VSL and the TC regions is about 10η in the temporally developing jet.[28] Thus, the thickness of the TSL estimated from the mean enstrophy characteristics also agrees with the previous study on the TNTI.

Vorticity transport to the non-turbulent region causes the turbulent region to spread; this is related to the propagation of the irrotational boundary. Because of the propagation, fluids pass across the irrotational boundary. The non-turbulent fluid motion across the irrotational boundary is referred to as the local entrainment, which is caused by the propagation of the boundary toward the non-turbulent region. The propagation velocity of the irrotational boundary ($\mathbf{V}^P \equiv v_n \mathbf{n}$), which is the velocity of the local entrainment, is obtained from the enstrophy transport equation,[14]

$$v_n = \left(\frac{2\omega_i S_{ij} \omega_j}{|\nabla \omega^2|} + \frac{2\nu \omega_i \nabla^2 \omega_i}{|\nabla \omega^2|} \right) = v_P + v_{Vis}. \tag{8}$$

Note that $\mathbf{V}^P$ is the velocity of the movement of the irrotational boundary relative to the fluid element at which the boundary is located. Equation (8) is derived by considering Eq. (7) on the enstrophy isosurface. A positive value of v_n represents the propagation of the irrotational boundary toward the non-turbulent region. The propagation velocities arising from the production term and the viscous terms are denoted by v_P and v_{Vis}, respectively. The propagation velocity of the enstrophy isosurface strongly depends on the location of the isosurface within the TNTI, which is determined by the detection threshold.[28] Figure 5(b) shows the probability density functions (pdfs) of v_n, v_P, and v_{Vis} normalized by the Kolmogorov velocity $v_\eta = (\epsilon\nu)^{1/4}$. The irrotational boundary frequently propagates toward the non-turbulent region owing to the viscous effects because the irrotational boundary is located near the outer edge of the VSL. However, the boundary propagation towards the turbulent region ($v_n < 0$) is also observed. The contribution of the inviscid term v_P is very small. Thus, the pdfs of v_P and v_{Vis} also show that the isosurface of $|\boldsymbol{\omega}|\delta_U/\Delta U_0 = 0.08$ is located near the outer edge of the TNTI.

C. Scalar field near turbulent/non-turbulent interface

Figure 6 shows the instantaneous scalar profile and the detected irrotational boundary. The irrotational boundary seems to envelope the region of $0 < \phi < 1$; therefore, the location of the scalar interface, in which ϕ is adjusted between the outside and inside of the mixing layer, appears close to the TNTI. As Sc increases, smaller-scale scalar fluctuations are observed in the instantaneous profile.

The non-turbulent values of ϕ near the upper and lower TNTI are $\phi = 1$ and 0, respectively. Therefore, from the upper region, the passive scalar is entrained into the mixing layer while the scalar

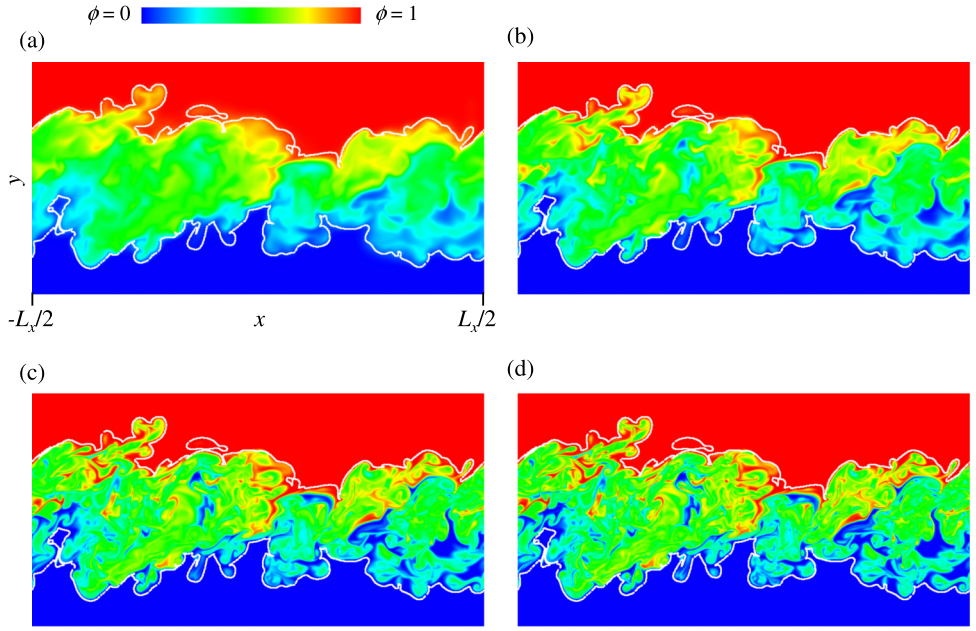

FIG. 6. Instantaneous scalar profile (color counter) and irrotational boundary (white line) on $x-y$ plane: (a) $Sc = 0.25$, (b) $Sc = 1$, (c) $Sc = 4$, and (d) $Sc = 8$. Part of the computational domain (region near the mixing layer) is visualized.

is diffused outwardly near the lower interface. It should be noted that both of the spreading and entrainment of the passive scalar are caused by the same physical processes, which should be explained by the transport by velocity and molecular diffusion in Eq. (5). In this study, the upper TNTI is analyzed to investigate the turbulent mixing near the interface, and we use ϕ for high Sc cases as a marker of the non-turbulent fluids. Because the gradient of the vorticity magnitude is opposite to that of ϕ for the upper TNTI, the irrotational boundary at which $\nabla|\omega| \cdot \nabla\phi < 0$ is used for calculating the conditional statistics for the upper interface. From the instantaneous scalar and enstrophy profiles and the location of the irrotational boundary, we confirmed that this method to distinguish the upper interface works well. Figure 7(a) shows the Schmidt number dependence of the conditional mean scalar profile. The change in $\langle\phi\rangle_I$ near the TNTI becomes steeper as Sc increases. However, the effect of Sc on $\langle\phi\rangle_I$ is not significant when Sc is high. Figure 7(b) shows the conditional average of the normalized scalar dissipation rate $\hat{N} = (1/ReSc)(\partial\phi/\partial\hat{x}_j)^2$, where $\hat{x} = x/\delta_{\omega 0}$. Similar to the previous DNS results,[33,39,40] the conditional mean scalar dissipation rate has a peak value in the turbulent region

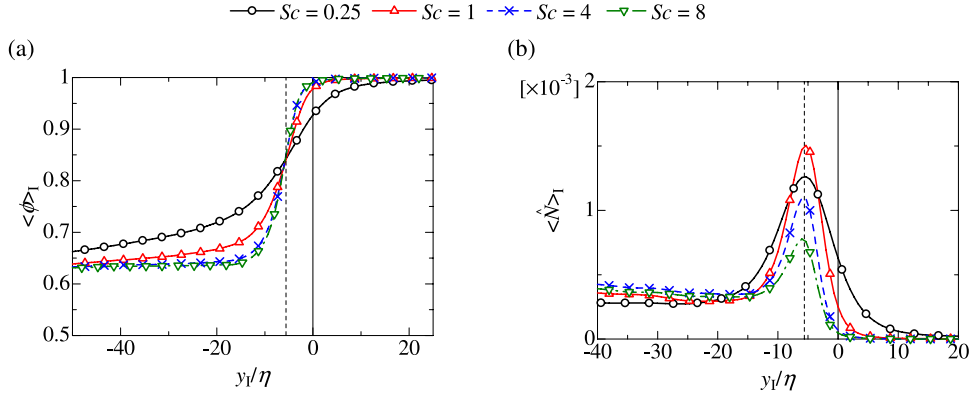

FIG. 7. Scalar characteristics near the upper TNTI for $Sc = 0.25$, 1, 4, and 8: (a) conditional mean scalar profile and (b) conditional mean scalar dissipation rate. The vertical broken line shows the location of a peak for the conditional mean scalar dissipation rate ($y_I/\eta = -5.6$).

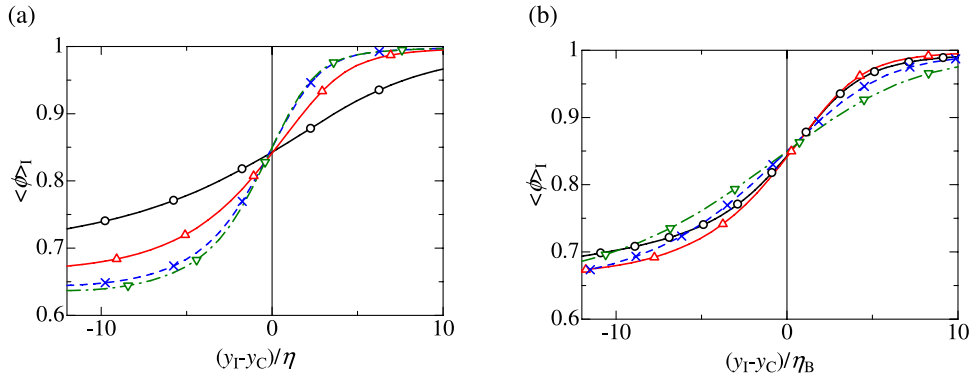

FIG. 8. Conditional mean scalar profile shown against the distance from the peak location of $\langle N \rangle_{\mathrm{I}}$ ($y_{\mathrm{C}}/\eta = -5.6$). The distance $y_{\mathrm{I}} - y_{\mathrm{C}}$ is normalized by (a) the Kolmogorov length scale η and (b) the Batchelor scale η_{B}. Symbols are the same as in Fig. 7.

near the TNTI. The location of the peak, which appears at $y_{\mathrm{I}} = -5.6\eta (= y_{\mathrm{C}})$ independently of Sc, is close to the boundary between the VSL and TSL ($y_{\mathrm{I}} \approx -5\eta$). The location of the peak is discussed in detail later in this paper. At this location, the profile of $\langle \phi \rangle_{\mathrm{I}}$ converges on $\langle \phi \rangle_{\mathrm{I}} = 0.84$ for all Sc. Thus, this location can be considered to be the center of the scalar interface, in which ϕ changes from the non-turbulent value to the turbulent value. The peak value becomes small as Sc increases for $Sc \geq 1$. Note that $(\partial\phi/\partial\hat{x}_j)^2$ increases with Sc and that the decrease in the peak value is caused by the large value of Sc. For $Sc = 0.25$, the peak is smaller than that for $Sc = 1$ because the molecular diffusion makes the scalar gradient small.

In Fig. 8, $\langle \phi \rangle_{\mathrm{I}}$ is replotted against the distance from the peak location of $\langle \hat{N} \rangle_{\mathrm{I}}$ ($y_{\mathrm{I}} - y_{\mathrm{C}}$, where $y_{\mathrm{C}} = -5.6\eta$) for examining the length scale which characterizes the width of the jump in $\langle \phi \rangle_{\mathrm{I}}$. Unless Sc is too small (much smaller than 0.25), the mean scalar profile across the mixing layer in Fig. 2(b) is independent of η_{B} because it does not depend on molecular diffusion and is determined by turbulent diffusion, which takes place at larger scales than the length scales of molecular diffusion.[41] Similarly, when Sc is so large that the length scale of molecular diffusion is much smaller than the thickness of the TNTI determined by the velocity field, the molecular diffusion is negligible in the conditional mean scalar profile near the TNTI. In contrast, for small Sc, the molecular diffusion acts over the TNTI layer and is enable to change the conditional mean scalar profile. We can find this tendency in Figs. 8(a) and 8(b). When the distance is normalized by the Kolmogorov length scale η, $\langle \phi \rangle_{\mathrm{I}}$ is similar for $Sc = 4$ and 8. However, the Batchelor scale η_{B} determines the width of the jump in $\langle \phi \rangle_{\mathrm{I}}$ for $Sc = 0.25$ and 1. Although the mean scalar profiles are less sensitive to higher Sc, Sc is expected to have a large influence on the instantaneous scalar profile within the TNTI layer, which will be confirmed in the probability density function of ϕ below.

According to Westerweel *et al.*,[13] the conditional mean streamwise velocity and scalar profiles, $\langle U \rangle_{\mathrm{I}}$ and $\langle \phi \rangle_{\mathrm{I}}$, are related to the turbulent Schmidt number $Sc_{\mathrm{T}} = \nu_e/D_e$ (ν_e: eddy viscosity and D_e: eddy diffusivity) by

$$\frac{\Delta U/U_S}{\Delta\phi/\phi_S} \approx Sc_{\mathrm{T}}, \tag{9}$$

where ΔU and $\Delta\phi$ are the magnitudes of the jumps in $\langle U \rangle_{\mathrm{I}}$ and $\langle \phi \rangle_{\mathrm{I}}$ across the TNTI layer and U_S and ϕ_S are the magnitudes of the changes in U and ϕ in the turbulent core region across the mixing layer. The jumps are estimated as the difference in $\langle U \rangle_{\mathrm{I}}$ and $\langle \phi \rangle_{\mathrm{I}}$ between $y_{\mathrm{I}}/\eta = 0$ and 40 because we can find a plateau region in $\langle \phi \rangle_{\mathrm{I}}$ around $y_{\mathrm{I}}/\eta = 40$. U_S and ϕ_S are estimated as the difference between $\langle U \rangle_{\mathrm{I}}$ ($\langle \phi \rangle_{\mathrm{I}}$) at $y_{\mathrm{I}}/\eta = 40$ and $\langle U \rangle$ ($\langle \phi \rangle$) on the centerline. With these estimations for $Sc = 4$, Eq. (9) yields $Sc_{\mathrm{T}} \approx 0.32$, which is close to the value in the round jet.[13] This agreement indicates that different flow configurations have only a small influence on the turbulent Schmidt number near the TNTI.

Figure 9 shows the structure of the large scalar dissipation rate and the irrotational boundary for $Sc = 1$ and 8. For both Schmidt numbers, sheetlike structures for a large scalar dissipation rate[42–45] are observed in the mixing layer. As confirmed in Figs. 9(c) and 9(d), as Sc increases, the thickness of

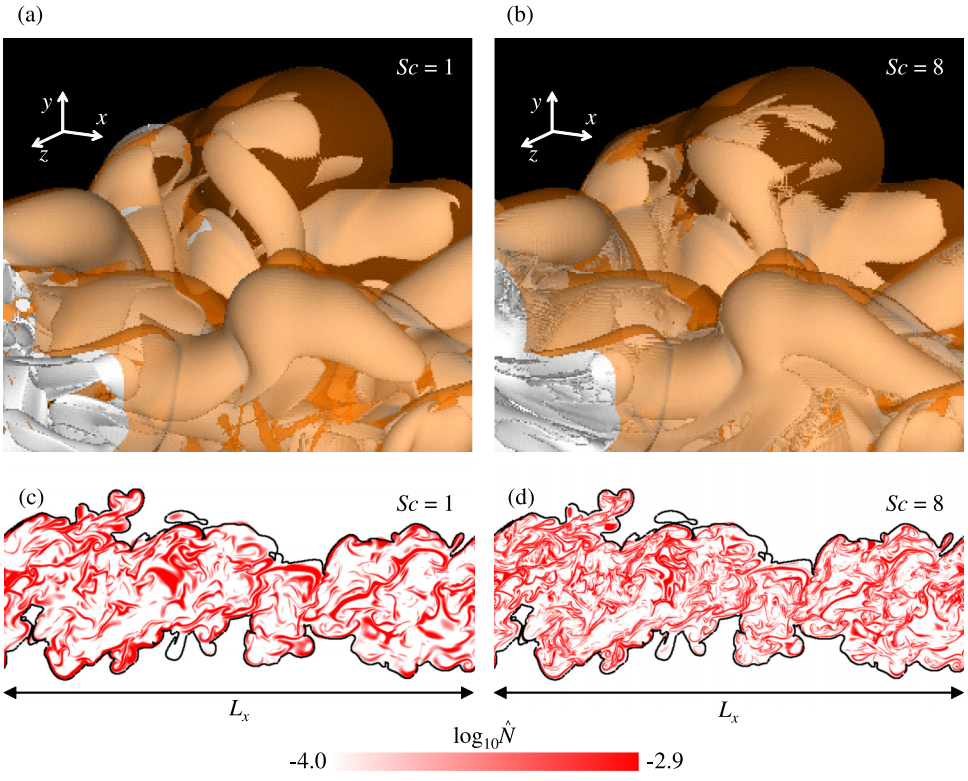

FIG. 9. Three-dimensional visualization of structure of large scalar dissipation rate (white) and irrotational boundary (translucent orange) for (a) $Sc = 1$ and (b) $Sc = 8$ at $t/T_{\mathrm{ref}} = 165.0$. In (a) and (b), the scalar dissipation structure is visualized by the isosurface of $\hat{N} = 1.25 \times 10^{-3}$. A small part of the computational domain is shown in (a) and (b). Scalar dissipation rate $\log_{10}\hat{N}$ (color counter) and irrotational boundary (black line) on x–y plane for (c) $Sc = 1$ and (d) $Sc = 8$. White: $\log_{10}\hat{N} \le -4.0$. Red: $\log_{10}\hat{N} \ge -2.9$.

the dissipation sheet decreases[44] while the number of sheetlike structures increases. Figures 9(a) and 9(b) visualize the scalar dissipation structure by the isosurface of $\hat{N} = 1.25 \times 10^{-3}$, which is close to the peak of $\langle \hat{N} \rangle_{\mathrm{I}}$ for $Sc = 1$. Figures 9(c) and 9(d) show the regions of $\hat{N} \ge 1.25 \times 10^{-3}$ in red. In these visualizations, the sheetlike structures are in both the TC region and the vicinity of the irrotational boundary. Therefore, the level of the scalar dissipation rate in the sheetlike structure in the TC region is comparable to that near the TNTI. However, $\langle \hat{N} \rangle_{\mathrm{I}}$ has a large peak within the TNTI. As confirmed in Fig. 9, the sheetlike structures exist intermittently in the TC region but frequently appear along the irrotational boundary. The peak of $\langle \hat{N} \rangle_{\mathrm{I}}$ is related to this tendency rather than the value of $\hat{N}$ in the sheetlike structure.

Figure 10 shows the change in the conditional pdf of ϕ across the irrotational boundary from the non-turbulent region ($y_{\mathrm{I}}/\eta = 6.7$) to the turbulent region ($y_{\mathrm{I}}/\eta = -11.1$) near the upper TNTI. At $y_{\mathrm{I}}/\eta = 6.7$, ϕ is equal to the non-turbulent value $\phi = 1$ except when $Sc = 0.25$. For the low Sc case, the molecular diffusion, which acts over a large distance, changes ϕ in the non-turbulent region near the irrotational boundary. At the irrotational boundary, the pdf has a large peak at $\phi = 1$ for $Sc = 4$ and 8. For $Sc = 1$, $\phi = 1$ is hardly observed at the irrotational boundary and ϕ is slightly smaller than the non-turbulent value. For $Sc = 4$ and 8, $\phi = 1$ is observed even in the turbulent region ($y_{\mathrm{I}}/\eta = -2.7, -5.6$, and -11.1). For these high Sc cases, a large peak for $\phi = 1$ does not exist at $y_{\mathrm{I}}/\eta = -11.1$, although the pdf for $\phi = 1$ still has a nonzero value. When a passive scalar is used to detect the TNTI, a scalar value slightly different from the non-turbulent value is used as the interface detection threshold. Figure 10(a) shows that the non-turbulent region with $\phi < 1$ is incorrectly detected as turbulent for low Sc when the passive scalar is used for the interface detection. On the other hand, ϕ can be a non-turbulent value even in the TSL for $Sc = 4$ and 8; the irrotational boundary, which is close to the edge of the VSL, cannot be detected using the scalar criteria for high Sc. A peak value of the pdf at $\phi = 1$ significantly decreases from $y_{\mathrm{I}}/\eta = -5.6$ to -11.1, and the boundary between the VSL and

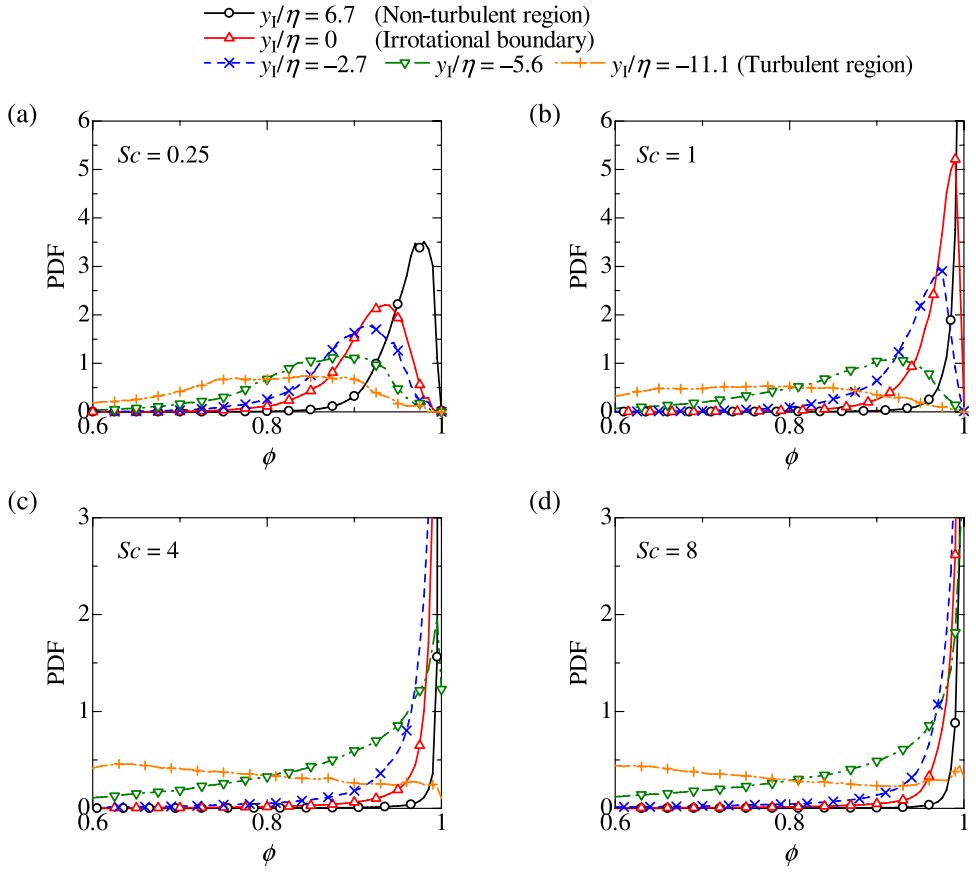

FIG. 10. Conditional pdf of scalar value near upper TNTI calculated at $y_I/\eta = 6.7$ (non-turbulent region), 0 (irrotational boundary), −2.7, −5.6, and −11.1 (turbulent region): (a) $Sc = 0.25$, (b) $Sc = 1$, (c) $Sc = 4$, and (d) $Sc = 8$.

TSL is expected to appear around $y_I/\eta = -5$. Therefore, the scalar isosurface for detecting the TNTI appears in the TSL when Sc is high. The change in the pdf across the TNTI shows that detection of the irrotational boundary using a passive scalar seems to work well only for $Sc = 1$ because the pdf has a large peak for ϕ slightly smaller than 1 at the irrotational boundary. Gampert *et al.*[33] also showed that the scalar isosurface is quite similar to the vorticity isosurface for $Sc = 1$.

Similar to the propagation velocity of the irrotational boundary, the propagation velocity for the isosurface of ϕ, which is relative to the flow velocity, is given by $v_n^\phi = D\nabla^2\phi/|\nabla\phi|$. We consider the isosurface of ϕ close to the non-turbulent values, which represents the outer edge of the scalar interface. The irrotational boundary propagation is dominated by the viscous effects, as shown in Fig. 5. Because the enstrophy and scalar isosurfaces are different from each other, we do not directly compare the two propagation velocities of these isosurfaces here. The propagation velocity of the irrotational boundary in Eq. (8) seems to be explicitly affected by the Reynolds number by the factor of $(1/Re)$, while the propagation velocity of the scalar isosurface is affected by $(1/ReSc)$. Thus, for low Sc cases, the propagation of the scalar isosurface can be faster than that of the irrotational boundary, and the scalar isosurface reaches outside of the irrotational boundary. In contrast, when Sc is high, the scalar isosurface propagates slowly and is located close to the TSL rather than the irrotational boundary. The pdf of ϕ also shows these tendencies of the scalar isosurface location relative to the irrotational boundary.

D. Passive scalar transport near turbulent/non-turbulent interface

When the scalar transport near the TNTI is considered, the TNTI movement should be taken into account. We introduce a local coordinate system which moves with the irrotational boundary

and is represented by $\mathbf{x}^{\mathrm{I}}$.[29] The origin of $\mathbf{x}^{\mathrm{I}}$ is located on the irrotational boundary. The coordinate system $\mathbf{x}$, whose origin is located at the center of the computational domain, is referred to as a fixed coordinate system hereafter. We also use t and t' to represent time in the fixed and local coordinate systems, respectively. The location of $\mathbf{x} = \mathbf{x}_0^{\mathrm{I}}$ in the fixed coordinate system is assumed to be located on the irrotational boundary and is used as the origin of the local coordinate system. The velocity of the movement of the irrotational boundary at $\mathbf{x} = \mathbf{x}_0^{\mathrm{I}}$, which is denoted as $\mathbf{U}^{\mathrm{I}}$, is given by the sum of the fluid velocity and the propagation velocity: $\mathbf{U}^{\mathrm{I}} = \mathbf{U}(\mathbf{x}_0^{\mathrm{I}}) + \mathbf{V}^{\mathrm{P}}$.[14] By considering the coordinate transformation from the fixed coordinate system $(\mathbf{x},t)$ to the local coordinate system $(\mathbf{x}^{\mathrm{I}},t')$, the passive scalar transport equation in the local coordinate system can be derived,[29]

$$\frac{\partial \phi}{\partial t'} = -\left(\mathbf{U}(\mathbf{x}^{\mathrm{I}} + \mathbf{x}_0^{\mathrm{I}}) - \mathbf{U}^{\mathrm{I}}\right) \cdot \nabla \phi + D\nabla^2 \phi. \tag{10}$$

The first term on the right-hand side in Eq. (10) represents the transport of ϕ due to the relative velocity $\Delta\mathbf{U}^{\mathrm{I}} \equiv (\mathbf{U} - \mathbf{U}^{\mathrm{I}})$ in the local coordinate system and the second term is the molecular diffusion term. The relative velocity can be written by $\mathbf{U}(\mathbf{x}^{\mathrm{I}} + \mathbf{x}_0^{\mathrm{I}}) - \mathbf{U}^{\mathrm{I}} = \mathbf{U}(\mathbf{x}^{\mathrm{I}} + \mathbf{x}_0^{\mathrm{I}}) - \mathbf{U}(\mathbf{x}_0^{\mathrm{I}}) - \mathbf{V}^{\mathrm{P}}$ and is determined by the fluid velocity difference $\mathbf{U}(\mathbf{x}^{\mathrm{I}} + \mathbf{x}_0^{\mathrm{I}}) - \mathbf{U}(\mathbf{x}_0^{\mathrm{I}})$ and the propagation velocity $\mathbf{V}^{\mathrm{P}}$. Although the fluid velocity difference has a large contribution to the relative velocity away from the irrotational boundary, it can be neglected in the region very close to the irrotational boundary.[46] The transport term due to the relative velocity includes the advection of fluid element containing a scalar by the velocity field and the effect of the irrotational boundary propagation. The latter arises from the viscous effects as confirmed in Fig. 5 and is not an actual "advection" term. The relative velocity can be decomposed into the boundary normal component $\Delta\mathbf{U}_{\mathrm{N}}^{\mathrm{I}} \equiv (\Delta\mathbf{U}^{\mathrm{I}} \cdot \mathbf{n})\mathbf{n}$ and tangential component $\Delta\mathbf{U}_{\mathrm{T}}^{\mathrm{I}} \equiv \Delta\mathbf{U}^{\mathrm{I}} - \Delta\mathbf{U}_{\mathrm{N}}^{\mathrm{I}}$. Then, the scalar transport by the relative velocity can also be decomposed into the two components,

$$-\left(\mathbf{U} - \mathbf{U}^{\mathrm{I}}\right) \cdot \nabla \phi = -\Delta\mathbf{U}_{\mathrm{N}}^{\mathrm{I}} \cdot \nabla \phi - \Delta\mathbf{U}_{\mathrm{T}}^{\mathrm{I}} \cdot \nabla \phi. \tag{11}$$

At the irrotational boundary, the transport by the relative velocity is determined solely by the propagation velocity of the irrotational boundary and is represented by

$$-\left(\mathbf{U} - \mathbf{U}^{\mathrm{I}}\right) \cdot \nabla \phi = \mathbf{V}^{\mathrm{P}} \cdot \nabla \phi \quad \text{(at the irrotational boundary)}. \tag{12}$$

The role of the propagation can be found from the conditional mean scalar profile in Fig. 7(a). Near the upper interface, ϕ increases toward the non-turbulent region. Therefore, when the irrotational boundary propagates toward the non-turbulent region, ϕ at the irrotational boundary increases because the irrotational boundary moves to the location of larger ϕ.[29] In contrast, the propagation towards the turbulent region, which does not frequently occur as shown in Fig. 5(b), causes ϕ to decrease at the irrotational boundary.

Figure 11 compares the conditional average of Eq. (10) for $Sc = 0.25$, 1, and 8. The transport term by the relative velocity is computed separately for the normal and tangential components of the irrotational boundary. First, we compare the molecular diffusion term. For $Sc = 0.25$ and 1, the molecular diffusion term significantly contributes to the decrease in ϕ in the non-turbulent region. However, the conditional mean molecular diffusion term is very small in the non-turbulent region for $Sc = 8$ and has nonzero values only in the turbulent region. Thus, for high Sc, the molecular diffusion changes the scalar value of fluid elements inside the irrotational boundary, while the scalars in the turbulent and non-turbulent regions can be mixed with each other for low Sc. The molecular diffusion contributes to the increase and decrease in ϕ in the regions $y_{\mathrm{I}}/\eta < -5.6$ and $-5.6 < y_{\mathrm{I}}/\eta$, respectively, and its effect becomes small as Sc increases. This profile of the molecular diffusion term corresponds to the conditional mean scalar profile in Fig. 7(a), which is smoothed by the molecular diffusion around $y_{\mathrm{I}} \approx -5.6\eta$. The conditional profile of the molecular diffusion term shows that the molecular diffusion exchanges the scalar between the VSL and TSL. Regarding the transport by the relative velocity, the tangential component is very small compared with the normal component near the irrotational boundary; therefore, the molecular diffusion and normal transport term by the relative velocity contribute to the temporal variation of ϕ on average. These two terms have large nonzero values near the irrotational boundary for $Sc = 0.25$ and 1. The molecular diffusion has a larger contribution at $Sc = 0.25$ than the transport by the relative velocity, and this results in a slow decrease in ϕ (negative $\langle \partial\phi/\partial t' \rangle_{\mathrm{I}}$) near the irrotational boundary. Thus, $\langle \phi \rangle_{\mathrm{I}}$ for $Sc = 0.25$ is slightly smaller than

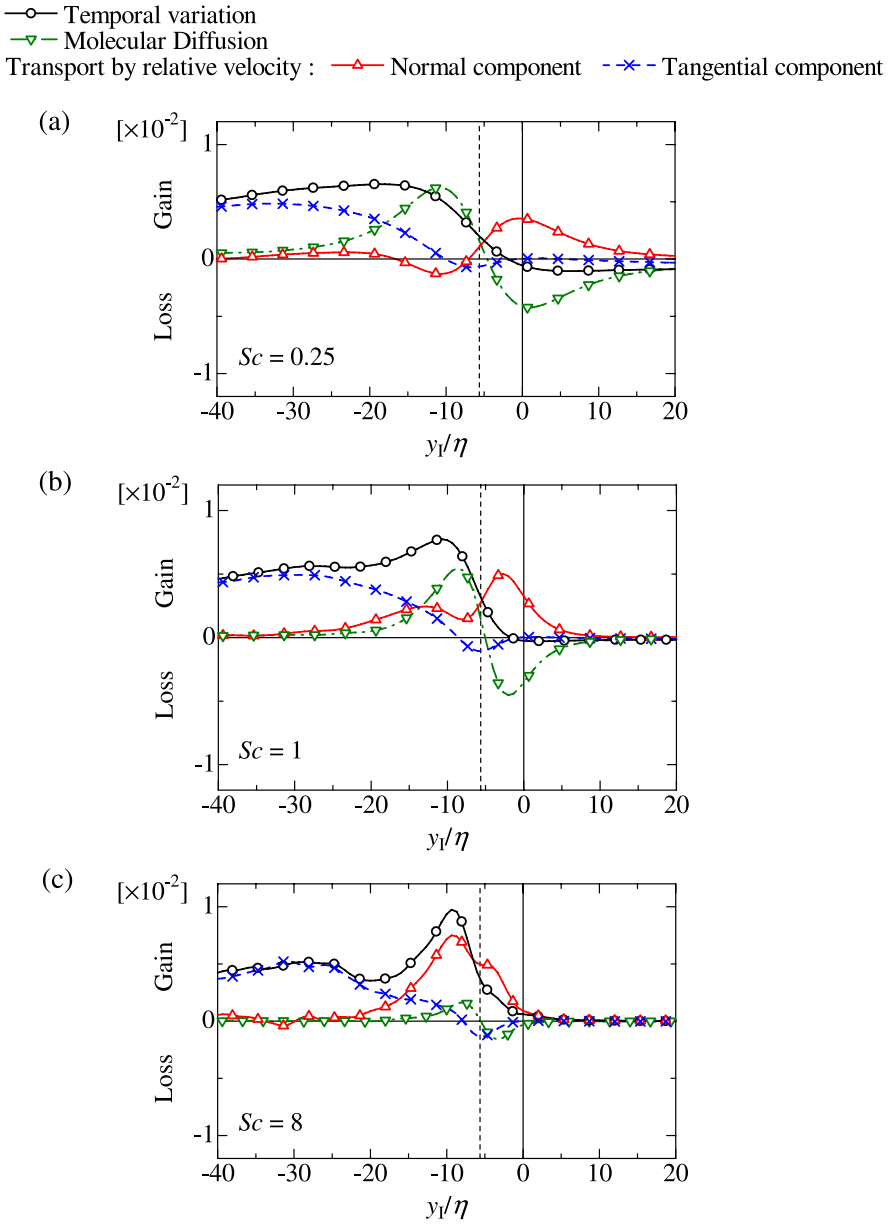

FIG. 11. Conditional average of scalar transport equation in local coordinate system near upper TNTI: (a) $Sc = 0.25$, (b) $Sc = 1$, and (c) $Sc = 8$. The scalar transport equation is normalized by $\delta_{\omega 0}$ and ΔU_0. The vertical broken line shows the location of a peak of the conditional mean scalar dissipation rate ($y_I/\eta = -5.6$).

1 even in the non-turbulent region near the irrotational boundary. As shown in Fig. 7(a), for both $Sc = 1$ and 8, $\langle\phi\rangle_I$ at the irrotational boundary is close to the non-turbulent value. However, this is caused by a different reason, as explained below. For $Sc = 1$ in Fig. 11(b), small temporal variation in ϕ is caused by balance between the molecular diffusion term and the effect of the propagation of irrotational boundary.[29] For $Sc = 8$, both the molecular diffusion and transport by the relative velocity hardly change ϕ near the irrotational boundary because of the high Sc and the small gradient of ϕ at the irrotational boundary. Thus, ϕ near the irrotational boundary stays at $\phi \approx 1$.

Although the scalar interface appears near the irrotational boundary, the difference between the two different interfaces can be seen in the visualization in Fig. 6. For higher Sc, the thin layers of $\phi \approx 0$ and 1 are more clearly seen slightly inside the lower and upper irrotational boundaries, respectively. This observation agrees with the conditional pdf of ϕ. The conditional profiles of Fig. 11 show that

the fluid elements near the irrotational boundary are less affected by the molecular diffusion at higher Sc. The passive scalar in a fluid element, which is advected by the velocity field, is changed only by the molecular diffusion.[47] Therefore, ϕ of the entrained fluid elements stays at the non-turbulent value for high Sc even in the turbulent region near the irrotational boundary.

The scalar transport equation in Eq. (10) can be rewritten by the divergence of the scalar fluxes as follows:

$$\frac{\partial \phi}{\partial t'} = -\nabla \cdot \left(\Delta \mathbf{U}_{\mathrm{N}}^{\mathrm{I}} \phi + \Delta \mathbf{U}_{\mathrm{T}}^{\mathrm{I}} \phi - D \nabla \phi \right). \tag{13}$$

The flux by the relative velocity normal to the irrotational boundary is represented by $\Delta \mathbf{U}_{\mathrm{N}}^{\mathrm{I}} \phi = f_{\mathrm{V}}^{\mathrm{N}} \mathbf{n}$ and $f_{\mathrm{V}}^{\mathrm{N}} \equiv (\Delta \mathbf{U}_{\mathrm{N}}^{\mathrm{I}} \cdot \mathbf{n}) \phi$. Because the direction of the tangential component is arbitrarily oriented on the plane parallel to the irrotational boundary, we use the magnitude of the tangential flux $|f_{\mathrm{V}}^{\mathrm{T}}| \equiv |\Delta \mathbf{U}_{\mathrm{T}}^{\mathrm{I}} \phi|$ to investigate the scalar transport process near the TNTI. The molecular diffusion flux $-D \nabla \phi$ is also decomposed into the normal and tangential components. Similar to the flux by the relative velocity, the normal flux by the molecular diffusion is represented by $f_{\mathrm{M}}^{\mathrm{N}} \mathbf{n}$ and $f_{\mathrm{M}}^{\mathrm{N}} \equiv -D \nabla \phi \cdot \mathbf{n}$.

First, we investigate the scalar flux normal to the irrotational boundary near the upper TNTI $(f_{\mathrm{V}}^{\mathrm{N}} + f_{\mathrm{M}}^{\mathrm{N}}) \cdot \mathbf{n}$. At $y_{\mathrm{I}} = 0$, it represents the scalar transfer across the irrotational boundary. Note that $f_{\mathrm{V}}^{\mathrm{N}}$ at the irrotational boundary is given by $-v_{\mathrm{n}} \phi$ and is the scalar transfer by the propagation of the irrotational boundary. In the present definition of the scalar flux, a negative value for $f_{\mathrm{V}}^{\mathrm{N}} + f_{\mathrm{M}}^{\mathrm{N}}$ denotes the scalar transfer toward the TC region. Figure 12(a) shows the mean values of the total flux $f_{\mathrm{V}}^{\mathrm{N}} + f_{\mathrm{M}}^{\mathrm{N}}$, the relative velocity flux $f_{\mathrm{V}}^{\mathrm{N}}$, and the molecular diffusion flux $f_{\mathrm{M}}^{\mathrm{N}}$ at the irrotational boundary for different Sc. The mean scalar fluxes are negative, and the scalar in the non-turbulent region is transferred across the upper irrotational boundary by the propagation of the irrotational boundary and molecular diffusion. As Sc decreases, the contributions of the boundary propagation and molecular diffusion decrease and increase, respectively; therefore, the total mean scalar flux stays almost constant. Even for $Sc = 0.25$, the molecular diffusion flux accounts for only 12.8% of the mean total flux. Thus, the scalar is transferred across the upper irrotational boundary by the propagation of the irrotational boundary rather than the molecular diffusion, especially for $Sc \geq 1$. It should be noted that the scalar flux itself does not represent the change in ϕ, and the molecular diffusion term in Eq. (10) largely contributes to the change in ϕ near the irrotational boundary as shown in Fig. 11. Figure 12(b) shows the pdf of $f_{\mathrm{V}}^{\mathrm{N}} = -v_{\mathrm{n}} \phi$ at the irrotational boundary. Because of the propagation to the non-turbulent region ($v_{\mathrm{n}} > 0$), the scalar in the non-turbulent region is frequently transferred across the upper irrotational boundary ($f_{\mathrm{V}}^{\mathrm{N}} < 0$). However, the opposite movement of the irrotational boundary ($v_{\mathrm{n}} < 0$) is also observed. When the irrotational boundary propagates toward the turbulent region, the fluid with a turbulent scalar value ($0 < \phi < 1$) is left in the non-turbulent region ($f_{\mathrm{V}}^{\mathrm{N}} > 0$). This scalar transport from the turbulent region was also observed in a planar jet.[29]

After the non-turbulent fluid crosses the irrotational boundary, it is transferred toward the TC region across the TNTI. For further investigation of the entrainment of fluid elements containing a

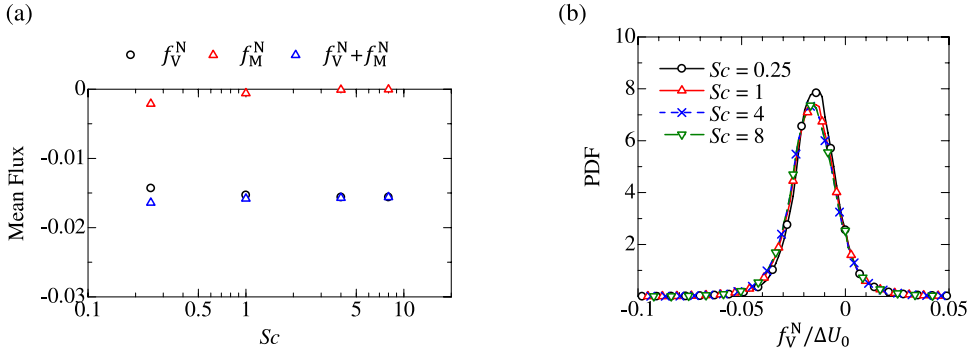

FIG. 12. Dependence of scalar flux across upper irrotational boundary on Sc: (a) mean scalar fluxes due to propagation of irrotational boundary and molecular diffusion and (b) pdf of scalar flux due to propagation of irrotational boundary. The scalar fluxes are normalized by ΔU_0.

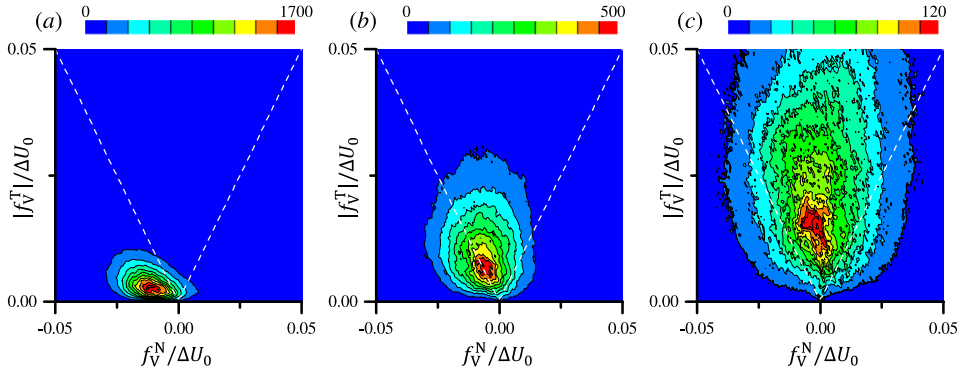

FIG. 13. Conditional joint pdf of scalar fluxes by relative velocity normal and tangential to irrotational boundary (f_V^N and $|f_V^T|$) in turbulent region near upper TNTI ($Sc = 1$): (a) $y_I/\eta = -2.7$, (b) $y_I/\eta = -5.6$, and (c) $y_I/\eta = -11.1$. The white broken line denotes $|f_V^T| = |f_V^N|$.

scalar near the TNTI, we analyze the relationship between the scalar fluxes due to the boundary normal and tangential components of the relative velocity. Figure 13 shows the conditional joint pdf of f_V^N and $|f_V^T|$ calculated at several locations away from the irrotational boundary in the turbulent region. At $y_I/\eta = -2.7$ (Fig. 13(a)), the joint pdf shows a preference for $f_V^N < 0$ and $|f_V^N| > |f_V^T|$. Thus, the fluid with the scalar is further transferred toward the TC region in the direction normal to the irrotational boundary. The scalar transfer toward the irrotational boundary, which is represented by positive f_V^N, hardly occurs at $y_I/\eta = -2.7$. As the fluid moves away from the irrotational boundary, $|f_V^T|$ becomes large, and the peak of the joint pdf becomes close to $f_V^N = 0$. Thus, at $y_I/\eta = -5.6$ and -11.1, the scalar is transferred in the tangential direction of the irrotational boundary rather than the normal direction ($|f_V^N| < |f_V^T|$). In Fig. 13, a large tangential scalar flux is observed from $y_I \approx -5\eta$, which is within the TSL, although the scalar flux in the normal direction is large in the VSL ($-5\eta \le y_I \le 0$).

These scalar fluxes are the result of the transport of fluid elements containing the scalar. The conditional statistics of the scalar flux on y_I do not show the actual path of entrained fluid elements, which can be investigated by Lagrangian tracking of fluid particles.[15] However, taking into account the tendency that the fluid on y_I moves in the direction normal to the irrotational boundary at $y_I/\eta = -2.7$, we can consider that after the fluid passing across the irrotational boundary moves in the direction normal to the irrotational boundary, it moves in the direction tangential to the boundary. From the change in the conditional joint pdf with y_I, we can describe the turbulent mixing near the TNTI, as shown in Fig. 14. The first stage of the turbulent mixing takes place in the VSL (Fig. 14(a)). The non-turbulent fluid near the irrotational boundary (shown in red) becomes turbulent by the viscous diffusion of vorticity and is locally entrained across the irrotational boundary. Because of the propagation of the irrotational boundary, the fluid element coming from the non-turbulent region moves away from the irrotational boundary in the VSL in the normal direction of the irrotational boundary. From a small probability for positive f_V^N at $y_I/\eta = -2.7$ in Fig. 13(a), it is found that the fluid element hardly moves toward the irrotational boundary in the VSL. This fluid movement in the normal direction is caused by the pseudo advection by the propagation velocity, which is related to the viscous diffusion of vorticity. After this fluid reaches the TSL ($y_I \approx -5\eta$), it is transferred in the tangential direction of the irrotational boundary and is mixed with the fluid in the TC region (Fig. 14(b)). Taveira *et al.* also observed the tangential movements of fluid particles in the turbulent region near the TNTI.[15] da Silva *et al.* investigated the intense vorticity structure (IVS) near the TNTI in the jet and showed that the IVS does not exist in the turbulent region of $-5\eta \le y_I \le 0$ and appears in the region $y_I \le -5\eta$.[9] These results indicate that, as described in Fig. 14(b), the tangential transport of the entrained fluid is considered to be caused by turbulent motions such as IVSs within the TSL and that this fluid then moves into the TC region.

Because the fluid element hardly moves toward the irrotational boundary in the VSL, the VSL mostly consists of the fluid coming from the non-turbulent region, while the TSL contains fluids from both the non-turbulent and TC regions, which are drawn into the TSL from the VSL by the local

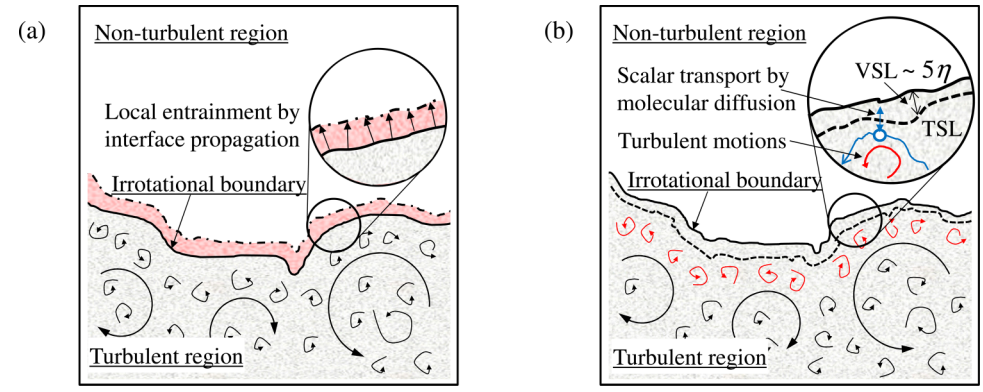

FIG. 14. Schematic of turbulent mixing caused by propagation of irrotational boundary in viscous superlayer (VSL), turbulent motions in turbulent sublayer (TSL), and molecular diffusion. (a) Local entrainment of non-turbulent fluids in VSL caused by propagation of irrotational boundary. The irrotational boundary propagates from the solid line to the dashed-dotted line, and the region shown in red is entrained into the turbulent region. (b) Transport by turbulent motions such as intense vorticity structure (IVS) (red) in TSL. Molecular diffusion contributes to the scalar transfer between the VSL and TSL, in which the turbulent motions transport a fluid element (shown by a blue circle and moving on a blue line) in the tangential direction of the irrotational boundary.

entrainment and from the TC region by the turbulent motions. This indicates that the fluid in the TC region can reach within the TSL but hardly moves into the VSL close to the irrotational boundary. The conditional pdf of ϕ for high Sc cases (Figs. 10(c) and 10(d)) also implies these different origins of fluids between the VSL and TSL. The scalar value near the TNTI can be used as a marker of the fluid element coming from the non-turbulent region for high Sc because the scalar value of the fluid element stays at the non-turbulent value ($\phi = 1$ near the upper interface) during the local entrainment of non-turbulent fluids. Therefore, the probability of $\phi \approx 1$ in Figs. 10(c) and 10(d) is interpreted as the probability that there is a fluid coming from the non-turbulent region by the local entrainment. The pdf of ϕ for $Sc = 4$ and 8 shows that the VSL ($-5\eta \le y_{\mathrm{I}} \le 0$) consists of the fluid from the non-turbulent region ($\phi = 1$), while both non-turbulent and turbulent values ($\phi = 1$ and $\phi < 1$, respectively) are observed in the TSL ($-14\eta \le y_{\mathrm{I}} \le -5\eta$). The shape of the pdf significantly changes from the VSL to the TSL. Because the molecular diffusion cannot be neglected even for $Sc = 8$ and the instantaneous thickness of the VSL can fluctuate, the conditional statistics of ϕ only provide a rough estimation on whether the fluids near the TNTI come from the non-turbulent region or the TC region. However, from the conditional pdf of ϕ, the origin of the fluid near the TNTI clearly changes around $y_{\mathrm{I}} = -5\eta$, which is close to the boundary between the TSL and VSL. Thus, the boundary between the TSL and VSL roughly separates the region (VSL) mostly consisting of the fluid from the non-turbulent flow from the region (TSL) in which the fluids from both the TC and non-turbulent regions coexist. Because of a large difference in ϕ between the fluids from the TC and non-turbulent regions, a large scalar gradient is expected to exist between the TSL and VSL. Because the locations of the TSL and VSL are independent of Sc, a peak value of the conditional mean scalar dissipation rate appears near the boundary between the TSL and VSL independently of Sc. As Sc increases, there is a sharp jump in $\langle\phi\rangle_{\mathrm{I}}$ in the thinner region around $y_{\mathrm{I}} = -5.6\eta$. However, the jump in $\langle\phi\rangle_{\mathrm{I}}$ is very similar for $Sc = 4$ and 8 although the molecular diffusion can smooth $\langle\phi\rangle_{\mathrm{I}}$. Therefore, the thickness of the jump in $\langle\phi\rangle_{\mathrm{I}}$ for high Sc might be determined by the fluctuation of instantaneous thickness of the VSL because the VSL thickness is related to the distance between the irrotational boundary and the fluid with a turbulent value of ϕ in the TSL.

When the passive scalar is supplied from the turbulent flow, the turbulent mixing processes described in Fig. 14 cause the outward spreading of the passive scalar, as observed for the lower side of the mixing layer. This situation is similar to the scalar transfer in the jet, in which the passive scalar is supplied from the jet inlet. The local entrainment of the non-turbulent fluids causes the outward movement of the VSL and TSL. Therefore, this local entrainment extends the region where the turbulent fluid can reach, and the turbulent motions then transport the fluids in the TC region into the TSL. Thus, the spreading of the passive scalar occurs because of the outward motion of the TNTI and the

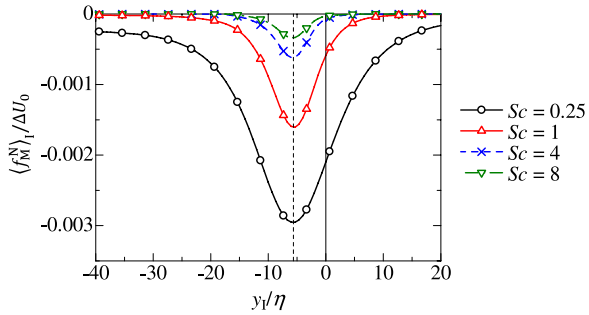

FIG. 15. Conditional mean scalar flux by molecular diffusion in the normal direction of irrotational boundary near the upper TNTI. The vertical broken line shows the location of a peak of the conditional mean scalar dissipation rate ($y_I/\eta = -5.6$).

turbulent motions in the TSL and TC regions. Note that the scalar transport near the upper and lower TNTI is dominated by the same processes consisting of the transport of fluid elements and molecular diffusion.

Figure 15 shows the conditional mean scalar flux by molecular diffusion in the normal direction of the irrotational boundary (f_M^N). The scalar flux by the molecular diffusion is represented by the scalar gradient, and similar to $\langle N \rangle_I$ in Fig. 7(b), it becomes large around the boundary between the VSL and TSL ($y_I/\eta \approx -5$) rather than at the irrotational boundary ($y_I = 0$). As can be seen in Fig. 15, the conditional mean scalar flux has a peak at $y_I/\eta = -5.6$, and the molecular diffusion largely contributes to the scalar transport from the VSL toward the TSL near the upper interface. Thus, the molecular diffusion exchanges the scalar between the VSL and TSL, as described in Fig. 14(b). The scalar flux by molecular diffusion is small compared with that due to the relative velocity in Fig. 13. For $Sc = 4$ and 8, the molecular diffusion term does not contribute to the scalar transport in the non-turbulent region. Although the molecular diffusion does not contribute to the scalar transport between the VSL and TSL as much as the relative velocity, it is not negligible for the low Sc cases. Because of the turbulent motions in the TSL and the absence in these motions in the VSL, the scalar transport between the VSL and TSL can be important to turbulent mixing. Near the upper interface, the fluid in the TSL acquires the scalar from the VSL owing to the molecular diffusion and is transported into the TC region. On the other hand, near the lower boundary, the molecular diffusion transfers the scalar from the TSL toward the VSL. Because the turbulent fluid in the TC region cannot reach deep inside of the VSL, the scalar transfer into the VSL near the lower boundary is caused by the molecular diffusion. Thus, the molecular diffusion acting between the VSL and TSL promotes the entrainment and spreading of the passive scalar due to turbulent mixing.

IV. CONCLUSION

We investigated the characteristics of the passive scalar and turbulent mixing near the TNTI by performing a DNS of the temporally developing mixing layer. Passive scalars with $Sc = 0.25$, 1, 4, and 8 were computed for one velocity field, and the Schmidt number dependence of passive scalar characteristics was investigated. For investigating the TNTI, we used the irrotational boundary, which is the isosurface of small vorticity magnitude located near the outer edge of the TNTI. We found that the engulfed fluid occupies only a very small part of the inner region of irrotational boundary envelope.

A sheetlike structure of a large scalar dissipation rate frequently appears near the TNTI, although the value of the scalar dissipation rate in this structure near the TNTI is comparable to that in the TC region. For low Sc cases, the molecular diffusion has a large influence on the scalar in both the turbulent and non-turbulent regions. In contrast, for high Sc cases, the non-turbulent fluid is entrained into the turbulent region without being significantly affected by the molecular diffusion. Therefore, the scalar isosurface used for detecting the TNTI are located outside and inside the irrotational boundary for low and high Sc, respectively. For high Sc cases, the scalar isosurface appears in the TSL rather than the VSL.

Unless the Schmidt number is quite low, turbulent mixing near the TNTI begins with the viscous diffusion of vorticity, which causes the non-turbulent fluids to cross the irrotational boundary (local entrainment). Once the non-turbulent fluid becomes turbulent at the irrotational boundary, the locally entrained fluid moves in the VSL towards the TC region in the normal direction of the irrotational boundary. As the fluid approaches the TSL, which is located about 5η away from the irrotational boundary, the fluid tends to be transferred in the tangential direction of the irrotational boundary rather than the normal direction.

This entrainment process and the scalar characteristics near the TNTI show that the boundary between the TSL and VSL separates the region (VSL) mostly consisting of the fluid coming from the non-turbulent flow from the region (TSL) in which the fluids from both the TC and non-turbulent regions coexist. Because of a large difference in a scalar between the VSL and TSL, the conditional mean scalar dissipation rate has a peak value at the location close to the boundary between the TSL and VSL independently of Sc, and the molecular diffusion exchanges the passive scalar between the VSL and TSL.

ACKNOWLEDGMENTS

The authors acknowledge Professor C. B. da Silva for providing valuable comments. The authors also acknowledge the anonymous referees for valuable comments. Part of this work was conducted under the Collaborative Research Project of the Institute of Fluid Science, Tohoku University. This work was supported by JSPS KAKENHI Grant No. 25002531 and MEXT KAKENHI Grant Nos. 25289030 and 25289031.

[1] P. E. Dimotakis, "Turbulent mixing," Annu. Rev. Fluid Mech. **37**, 329 (2005).
[2] J. C. Hill, "Homogeneous turbulent mixing with chemical reaction," Annu. Rev. Fluid Mech. **8**, 135 (1976).
[3] P. E. Dimotakis, "The mixing transition in turbulent flows," J. Fluid Mech. **409**, 69 (2000).
[4] C. B. da Silva, J. C. R. Hunt, I. Eames, and J. Westerweel, "Interfacial layers between regions of different turbulence intensity," Annu. Rev. Fluid Mech. **46**, 567 (2014).
[5] S. Corrsin and A. L. Kistler, "Free-stream boundaries of turbulent flows," NACA Technical Report No. TN-1244, 1955.
[6] C. B. da Silva, R. R. Taveira, and G. Borrell, "Characteristics of the turbulent/nonturbulent interface in boundary layers, jets and shear-free turbulence," J. Phys.: Conf. Ser. **506**, 012015 (2014).
[7] R. R. Taveira and C. B. da Silva, "Characteristics of the viscous superlayer in shear free turbulence and in planar turbulent jets," Phys. Fluids **26**, 021702 (2014).
[8] C. B. da Silva and R. R. Taveira, "The thickness of the turbulent/nonturbulent interface is equal to the radius of the large vorticity structures near the edge of the shear layer," Phys. Fluids **22**, 121702 (2010).
[9] C. B. da Silva, R. J. N. Dos Reis, and J. C. F. Pereira, "The intense vorticity structures near the turbulent/non-turbulent interface in a jet," J. Fluid Mech. **685**, 165 (2011).
[10] C. B. da Silva and R. J. N. dos Reis, "The role of coherent vortices near the turbulent/non-turbulent interface in a planar jet," Philos. Trans. R. Soc., A **369**, 738 (2011).
[11] J. Mathew and A. J. Basu, "Some characteristics of entrainment at a cylindrical turbulence boundary," Phys. Fluids **14**, 2065 (2002).
[12] J. Westerweel, C. Fukushima, J. M. Pedersen, and J. C. R. Hunt, "Mechanics of the turbulent-nonturbulent interface of a jet," Phys. Rev. Lett. **95**, 174501 (2005).
[13] J. Westerweel, C. Fukushima, J. M. Pedersen, and J. C. R. Hunt, "Momentum and scalar transport at the turbulent/non-turbulent interface of a jet," J. Fluid Mech. **631**, 199 (2009).
[14] M. Holzner and B. Lüthi, "Laminar superlayer at the turbulence boundary," Phys. Rev. Lett. **106**, 134503 (2011).
[15] R. R. Taveira, J. S. Diogo, D. C. Lopes, and C. B. da Silva, "Lagrangian statistics across the turbulent-nonturbulent interface in a turbulent plane jet," Phys. Rev. E **88**, 043001 (2013).
[16] J. Philip and I. Marusic, "Large-scale eddies and their role in entrainment in turbulent jets and wakes," Phys. Fluids **24**, 055108 (2012).
[17] K. Chauhan, J. Philip, C. M. de Silva, N. Hutchins, and I. Marusic, "The turbulent/non-turbulent interface and entrainment in a boundary layer," J. Fluid Mech. **742**, 119 (2014).
[18] C. M. de Silva, J. Philip, K. Chauhan, C. Meneveau, and I. Marusic, "Multiscale geometry and scaling of the turbulent-nonturbulent interface in high Reynolds number boundary layers," Phys. Rev. Lett. **111**, 044501 (2013).
[19] J. Philip, C. Meneveau, C. M. de Silva, and I. Marusic, "Multiscale analysis of fluxes at the turbulent/non-turbulent interface in high Reynolds number boundary layers," Phys. Fluids **26**, 015105 (2014).
[20] R. A. Antonia, "Conditional sampling in turbulence measurement," Annu. Rev. Fluid Mech. **13**, 131 (1981).
[21] J. Westerweel, T. Hofmann, C. Fukushima, and J. C. R. Hunt, "The turbulent/non-turbulent interface at the outer boundary of a self-similar turbulent jet," Exp. Fluids **33**, 873 (2002).
[22] R. K. Anand, B. J. Boersma, and A. Agrawal, "Detection of turbulent/non-turbulent interface for an axisymmetric turbulent jet: Evaluation of known criteria and proposal of a new criterion," Exp. Fluids **47**, 995 (2009).
[23] T. Watanabe, T. Naito, Y. Sakai, K. Nagata, and Y. Ito, "Mixing and chemical reaction at high schmidt number near turbulent/nonturbulent interface in planar liquid jet," Phys. Fluids **27**, 035114 (2015).

[24] M. Gampert, K. Kleinheinz, N. Peters, and H. Pitsch, "Experimental and numerical study of the scalar turbulent/non-turbulent interface layer in a jet flow," Flow, Turbul. Combust. **92**, 429 (2014).
[25] M. Holzner, A. Liberzon, N. Nikitin, B. Lüthi, W. Kinzelbach, and A. Tsinober, "A Lagrangian investigation of the small-scale features of turbulent entrainment through particle tracking and direct numerical simulation," J. Fluid Mech. **598**, 465 (2008).
[26] M. Wolf, B. Lüthi, M. Holzner, D. Krug, W. Kinzelbach, and A. Tsinober, "Investigations on the local entrainment velocity in a turbulent jet," Phys. Fluids **24**, 105110 (2012).
[27] M. Wolf, M. Holzner, B. Lüthi, D. Krug, W. Kinzelbach, and A. Tsinober, "Effects of mean shear on the local turbulent entrainment process," J. Fluid Mech. **731**, 95 (2013).
[28] M. van Reeuwijk and M. Holzner, "The turbulence boundary of a temporal jet," J. Fluid Mech. **739**, 254 (2014).
[29] T. Watanabe, Y. Sakai, K. Nagata, Y. Ito, and T. Hayase, "Enstrophy and passive scalar transport near the turbulent/non-turbulent interface in a turbulent planar jet flow," Phys. Fluids **26**, 105103 (2014).
[30] T. Watanabe, Y. Sakai, K. Nagata, Y. Ito, and T. Hayase, "Wavelet analysis of coherent vorticity near the turbulent/non-turbulent interface in a turbulent planar jet," Phys. Fluids **26**, 095105 (2014).
[31] M. M. Rogers and R. D. Moser, "Direct simulation of a self-similar turbulent mixing layer," Phys. Fluids **6**, 903 (1994).
[32] M. Tanahashi, S. Iwase, and T. Miyauchi, "Appearance and alignment with strain rate of coherent fine scale eddies in turbulent mixing layer," J. Turbul. **2**, 1 (2001).
[33] M. Gampert, J. Boschung, F. Hennig, M. Gauding, and N. Peters, "The vorticity versus the scalar criterion for the detection of the turbulent/non-turbulent interface," J. Fluid Mech. **750**, 578 (2014).
[34] A. Kempf, M. Klein, and J. Janicka, "Efficient generation of initial-and inflow-conditions for transient turbulent flows in arbitrary geometries," Flow, Turbul. Combust. **74**, 67 (2005).
[35] H. Suzuki, K. Nagata, Y. Sakai, T. Hayase, Y. Hasegawa, and T. Ushijima, "An attempt to improve accuracy of higher-order statistics and spectra in direct numerical simulation of incompressible wall turbulence by using the compact schemes for viscous terms," Int. J. Numer. Methods Fluids **73**, 509 (2013).
[36] Y. Morinishi, T. S. Lund, O. V. Vasilyev, and P. Moin, "Fully conservative higher order finite difference schemes for incompressible flow," J. Comput. Phys. **143**, 90 (1998).
[37] P. R. Spalart, R. D. Moser, and M. M. Rogers, "Spectral methods for the Navier-Stokes equations with one infinite and two periodic directions," J. Comput. Phys. **96**, 297 (1991).
[38] R. R. Taveira and C. B. da Silva, "Kinetic energy budgets near the turbulent/nonturbulent interface in jets," Phys. Fluids **25**, 015114 (2013).
[39] R. R. Taveira, C. B. da Silva, and J. C. F. Pereira, "The dynamics of turbulent scalar mixing near the edge of a shear layer," J. Phys.: Conf. Ser. **318**, 052049 (2011).
[40] A. Attili, J. C. Cristancho, and F. Bisetti, "Statistics of the turbulent/non-turbulent interface in a spatially developing mixing layer," J. Turbul. **15**, 555 (2014).
[41] S. B. Pope, *Turbulent Flows* (Cambridge University Press, 2000).
[42] K. A. Buch and W. J. A. Dahm, "Experimental study of the fine-scale structure of conserved scalar mixing in turbulent shear flows. Part 1. Sc $\gg$ 1," J. Fluid Mech. **317**, 21 (1996).
[43] L. K. Su and N. T. Clemens, "Planar measurements of the full three-dimensional scalar dissipation rate in gas-phase turbulent flows," Exp. Fluids **27**, 507 (1999).
[44] L. K. Su and N. T. Clemens, "The structure of fine-scale scalar mixing in gas-phase planar turbulent jets," J. Fluid Mech. **488**, 1 (2003).
[45] J. Schumacher, K. R. Sreenivasan, and P. K. Yeung, "Very fine structures in scalar mixing," J. Fluid Mech. **531**, 113 (2005).
[46] T. Watanabe, Y. Sakai, K. Nagata, Y. Ito, and T. Hayase, "Vortex stretching and compression near the turbulent/nonturbulent interface in a planar jet," J. Fluid Mech. **758**, 754 (2014).
[47] R. O. Fox, *Computational Models for Turbulent Reacting Flows* (Cambridge University Press, 2003).